Isotope shift measurements in the $2s_{1/2} \rightarrow 2p_{3/2}$ transition of Be^{+} and extraction of the nuclear charge radii for $^{7,\,10,\,11}Be$

2010 J. Phys. G: Nucl. Part. Phys. 37 055107

(http://iopscience.iop.org/0954-3899/37/5/055107)

J. Phys. G: Nucl. Part. Phys. **37** (2010) 055107 (14pp) doi:10.1088/0954-3899/37/5/055107

Isotope shift measurements in the $2s_{1/2} \rightarrow 2p_{3/2}$ transition of Be^+ and extraction of the nuclear charge radii for $^{7,10,11}Be$

M Žáková[1], Z Andjelkovic[1], M L Bissell[2], K Blaum[3], G W F Drake[4], Ch Geppert[5,6], M Kowalska[7], J Krämer[1], A Krieger[1], M Lochmann[1], T Neff[5], R Neugart[8], W Nörtershäuser[1,5], R Sánchez[1,5], F Schmidt-Kaler[9], D Tiedemann[1], Z-C Yan[10], D T Yordanov[3] and C Zimmermann[6]

[1] Institut für Kernchemie, Universität Mainz, D-55128 Mainz, Germany
[2] Instituut voor Kern- en Stralingsfysica, Katholieke Universiteit Leuven, B-3001 Leuven, Belgium
[3] Max-Planck-Institut für Kernphysik, D-69117 Heidelberg, Germany
[4] Department of Physics, University of Windsor, Windsor, Ontario, N9B 3P4, Canada
[5] GSI Helmholtzzentrum für Schwerionenforschung GmbH, D-64291 Darmstadt, Germany
[6] Physikalisches Institut, Universität Tübingen, D-72076 Tübingen, Germany
[7] CERN, Physics Department, CH-1211 Geneva 23, Switzerland
[8] Institut für Physik, Universität Mainz, D-55099 Mainz, Germany
[9] Quanteninformationsverarbeitung, Universität Ulm, D-89069 Ulm, Germany
[10] Department of Physics, University of New Brunswick, Fredericton, New Brunswick, E3B 5A3, Canada

E-mail: w.noertershaeuser@uni-mainz.de

Received 8 January 2010
Published 1 April 2010
Online at stacks.iop.org/JPhysG/37/055107

Abstract

We have performed isotope shift measurements in the $2s_{1/2} \rightarrow 2p_{3/2}$ transition of Be^+ ions using advanced collinear laser spectroscopy with two counter-propagating laser beams. Measurements involving a frequency comb for laser stabilization and absolute frequency determination allowed us to determine the isotope shifts with an accuracy of 2 MHz. From the isotope shifts between ^9Be and $^{7,10,11}Be$, high-accuracy mass shift calculations and the charge radius of the reference isotope ^9Be we determined nuclear charge radii for the isotopes $^{7,10}Be$ and the one-neutron halo nucleus ^{11}Be. The results are compared to nuclear-structure calculations using the fermionic molecular dynamics model which reproduce well the general trend of the radii. Decreasing charge radii from ^7Be to ^{10}Be are explained by the cluster structure of the nuclei. The increase from ^{10}Be to ^{11}Be is mainly caused by the halo neutron by which the ^{10}Be core moves relative to the center of mass. Polarization of the ^{10}Be core has only a small influence on the charge radius.

(Some figures in this article are in colour only in the electronic version)

1. Introduction

Charge radii are among the basic properties of nuclei being used to test the predictions of nuclear structure models. Electron scattering experiments can to some degree provide the radial charge distribution and the nuclear charge radius, but they are not applicable for short-lived isotopes at present. For those, mainly two experimental approaches exist: nuclear reaction processes and optical precision spectroscopy. The matter radius can be extracted from nuclear interaction cross sections [1] and it was shown that the charge-changing cross sections show a Z dependence that is very similar to nuclear radii measured by electron scattering [2]. While charge-changing cross sections were investigated for nuclei close to the valley of stability [3] primarily for astrophysical applications, only a few attempts were made to extract charge distribution information for very exotic isotopes [4–6]. Isotope shift measurements using optical spectroscopy can provide nuclear-model-independent information on the nuclear charge radius and, thus, on the proton distribution in the nucleus. The comparison of charge and matter radii is particularly interesting in systems which show a strongly different distribution of protons and neutrons inside the nucleus. These are namely nuclei with a neutron or proton skin or a so-called halo. Halo nuclei were discovered by Tanihata *et al* in 1985 [1]. They performed nuclear reaction experiments with nuclei of light elements and observed significant changes in the interaction cross section between neighboring isotopes close to the neutron dripline. A notable increase for dripline nuclei was explained by a significantly extended matter distribution. It was proposed that this extension arises from weakly bound neutrons which form a region of diluted nuclear matter around a compact core with 'normal' nuclear density [7]. Since then, many experiments were carried out to understand the structure of these extraordinary systems. The most intensely studied halo nuclei are ^{6,8}He, ^{11}Li, ^{11}Be and ^{14}Be [8].

High-resolution optical spectroscopy [9] has considerably contributed to our understanding of halo nuclei. Collinear laser spectroscopy in combination with the β-NMR technique allowed the determination of the spin and the magnetic dipole moment of ^{11}Li [10] and ^{11}Be [11] as well as the determination of the electric quadrupole moment of ^{11}Li [12]. The results could be used to exclude a possible deformation of ^{11}Li because the spin $3/2$ belongs to a spherical state, the magnetic moment lies close to the Schmidt value and the quadrupole moment is similar to that of ^{9}Li. Both these values, which were improved recently [13, 14], again indicate that the nucleus is nearly spherical.

The question of charge radii in these exotic nuclei has been raised and highlighted as important for a better understanding of the interaction between halo and core. At present only two groups have succeeded in measuring nuclear charge radii of the light halo systems in helium [15] and lithium [16] by high-precision laser spectroscopy. The extraction of nuclear charge radii from these isotope-shift measurements had become only possible because the mass-dependent part of the isotope shift could be calculated with sufficiently high accuracy, which is currently possible for atomic systems with up to three electrons. Yan and Drake published their first results with spectroscopic accuracy for transitions in lithium in 2000 [17] and the calculations have been continuously improved since then [18–21].

Standard collinear laser spectroscopy is not directly suitable for isotope shift measurements on the lightest elements. Until recently, ^{17}Ne was the lightest short-lived isotope for which so far charge radius information has been obtained using this technique [22]. The reason for that is an insufficient accuracy in the acceleration voltage measurements. Consequently, the uncertainty of the Doppler shift of the fast ion beam by far exceeds the finite-size contribution to the isotope shift. This extremely small contribution of about 10^{-8} of the total transition frequency contains the essential information on the nuclear charge radius.

Recently, we described an advanced technique for spectroscopy on fast atoms and ions [23]. This approach combines collinear and anti-collinear laser spectroscopy and the absolute laser frequencies are determined with an accuracy better than 1 MHz employing a frequency comb. The technique was successfully applied for the measurements of the absolute transition frequencies in the $2s_{1/2} \rightarrow 2p_{1/2}$ transition of $^{7,9,10,11}Be^{+}$ ions [24]. In combination with accurate calculations of the mass-dependent isotope shift [20, 21] these transition frequencies were used to determine the changes in the mean-square nuclear charge radii along this chain of isotopes [23].

In the measurement presented here, we determine the isotope shifts in the $2s_{1/2} \rightarrow 2p_{3/2}$ transition with an accuracy of approximately 2 MHz, which is more than one order of magnitude better than that in [25]. This allows the extraction of the nuclear charge radii with an accuracy that is comparable to that in the D_1 line [23] and our results confirm the charge radii extracted from those. Additionally, the splitting isotope shift, i.e. the difference in the isotope shift between the two fine structure levels, was obtained and is compared to theoretical predictions which are nearly independent of both QED and nuclear volume effects. This provides a consistency check of the calculations as well as of the measurements.

Unlike binding energies, charge radii provide a direct test of the wavefunctions obtained from nuclear structure calculations. As charge radii are sensitive to the asymptotic behavior of the wavefunction, they can be related to the evolution of clustering or the development of halos. In this paper the measured charge radii are compared to recent no-core shell model (NCSM) results [26] and new calculations in the fermionic molecular dynamics (FMD) approach are presented.

2. Experimental setup

The experimental setup used for the isotope-shift measurements on beryllium isotopes has been described in previous publications [23, 27] and will be summarized here only briefly. The measurements were performed at the on-line isotope separator (ISOLDE) at CERN. Radioactive beryllium atoms, produced by 1.4 GeV proton-induced fragmentation reactions in a uranium carbide target, were ionized by resonance laser ionization (RILIS) and mass separated after acceleration to an energy of about 50 keV. A Be^{+} ion beam was then delivered to the beamline for collinear laser spectroscopy (COLLAPS) where it was superimposed with two laser beams: one in collinear and one in anti-collinear direction. Both lasers were locked at fixed frequencies, while the ion beam was accelerated or decelerated into the detection region by applying an additional high voltage between +10 kV and −10 kV. Resonance fluorescence was observed with photomultiplier tubes mounted at the beamline. The high voltage of ISOLDE and the voltage applied at the optical detection region were measured by utilising high-voltage dividers which were calibrated with a 1 ppm high-voltage divider developed and built at the University of Münster [28].

The final velocity of the ions shifts the rest-frame resonance frequency ν_0 in collinear and anti-collinear direction, respectively, to

$$\nu_c = \nu_0 \cdot \gamma \cdot (1 + \beta), \tag{1}$$

$$\nu_a = \nu_0 \cdot \gamma \cdot (1 - \beta), \tag{2}$$

with the time dilatation factor $\gamma = 1/\sqrt{1 - \beta^2}$. Changing the post-acceleration voltage at the detection region thus allows Doppler tuning of the effective frequencies ν_c and ν_a across the fixed laser frequency. The laser frequencies for collinear and anti-collinear excitation are chosen such that the hyperfine structure patterns are covered for both directions within a small

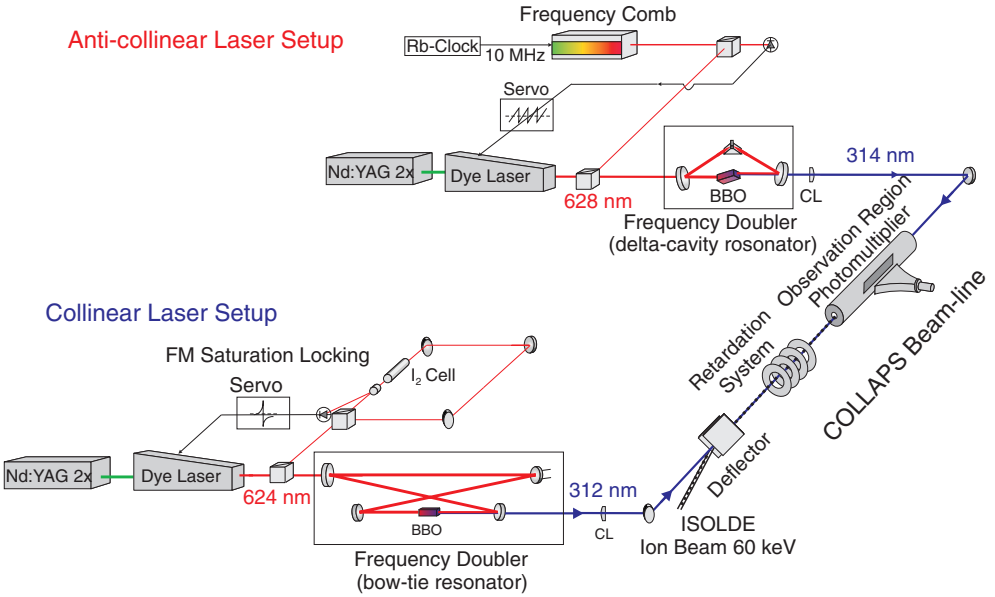

Figure 1. Simplified scheme of the experimental setup. The frequencies of the dye lasers for collinear and anti-collinear excitation were stabilized to a hyperfine transition of molecular iodine and to a frequency comb, respectively. The light from both lasers was frequency doubled and overlapped with the ion beam.

voltage range and that the centers of gravity (cg) almost coincide. With the cg coinciding for both laser beam directions the rest-frame transition frequency ν_0 can be determined solely from the laser frequencies according to

$$\nu_0^2 = \nu_c \cdot \nu_a. \tag{3}$$

A simplified scheme of the laser setup is shown in figure 1. Two cw-single-mode ring dye lasers (Coherent 699-21) with a linewidth of about 1 MHz were used to produce the fundamental wavelengths of 628 nm and 624 nm for anti-collinear and collinear excitation, respectively. The laser for collinear excitation was stabilized to a suitable iodine hyperfine transition while the other was directly locked to a fiber-laser-based frequency comb (Menlo Systems, FC1500). Therewith it was possible to determine the absolute laser frequencies with a relative accuracy of 10^{-9}. In total 12 iodine lines were chosen for the measurements. All lines are R branch lines with an even angular momentum J in the ground state. This is favorable, because they have a hyperfine structure exhibiting 15 components with the a_1 component well separated at the lower frequency side of the spectrum. This facilitates easy, reliable and reproducible locking during the beam time. The absolute locking frequencies for all selected iodine transitions were measured several times before, during and after the beam time with the frequency comb, to obtain accurate frequency information. For all lines very good agreement was found with the predicted frequencies from the iodine program IodineSpec (Toptica Photonics). In all cases deviations of less than 1 MHz were observed which is well below the quoted uncertainties of the calculated transition frequencies of a few MHz. The laser light was transported to the COLLAPS beamline by micro-structured fibers (LMA-20, Crystal Fibers). Two frequency doublers (SpectraPhysics Wavetrain and Tekhnoscan FD-SF-07) were used for the generation of ultraviolet light which is required for the $2s_{1/2} \rightarrow 2p_{3/2}$ transition in Be^+ (312 nm and 314 nm in collinear and anti-collinear direction, respectively). A power

of up to 15 mW was achieved in the ultraviolet, but for spectroscopy this was attenuated to values below 5 mW to avoid saturation effects.

The laser–laser and laser–ion beam overlap was optimized using two irises and a combination of small apertures with diameters down to 5 mm along the beamline. The irises could be closed during the alignment procedure to a diameter of 1 mm but were opened during measurements to avoid scattered light causing the additional background. Systematic uncertainties due to, e.g., the ion–laser and laser–laser beam misalignments, the ion and laser beam divergence or the momentum transfer to the ions by repetitive absorption of photons were investigated in an off-line test run on the stable ^{9}Be. The main source of systematic uncertainty of about 500 kHz was found to be a possible misalignment between the two laser beams. Concerning absolute transition frequencies, an additional uncertainty of about 800 kHz arises from the uncertainty of the Rb-clock that is used as a reference for the frequency comb. However, the latter can be neglected in isotope-shift measurements. It contributes to all isotopes with the same sign and similar size and largely cancels when the difference of the transition frequencies between two isotopes is calculated. All measurements were consecutively repeated several times. Collinear and anti-collinear spectra were recorded quasi-simultaneously by alternately blocking one of the laser beams in a fast sequence and scanning the Doppler tuning voltage across the resonances in typically 400 steps for the odd and 100 steps for the even isotopes. For one spectrum, 50–400 such scans, each taking about 4–8 s, were integrated depending on the production rate of the respective isotope. In total, 10–20 spectra with sufficient statistics were recorded for each isotope.

3. Experimental results

Figure 2 shows the collinear and anti-collinear spectra for ^{9}Be in the $2s_{1/2} \rightarrow 2p_{3/2}$ transition as a function of the applied tuning voltage. The observed peaks are labeled according to the respective $2s_{1/2}$ ground state hyperfine level F. The hyperfine structure in the upper $2p_{3/2}$ level is not resolved because the splitting is less than 10 MHz while the natural linewidth of the transition is 20 MHz. Furthermore, the observed linewidth in collinear spectroscopy is broadened to 50–70 MHz and, hence, only the ground state splitting is resolved, which ranges from 0.5–3.6 GHz for the different isotopes. The solid line represents a fit with a Voigt lineshape function and is discussed below. The dashed vertical lines mark the center of gravity voltages (U_{cg}) of both scans, which do not exactly coincide but are separated by ΔU_{cg} which amounts to a few volts.

The cg frequencies from the collinear and anti-collinear directions have to be combined to extract the rest-frame transition frequency. Since they do not appear at exactly the same acceleration voltage, the small correction ΔU_{cg} must be introduced for either one of the two spectra. First, the scaling factor k between voltage and frequency is determined for the acceleration voltage around the center of gravity. Depending on the isotope, this factor is between 30 and 40 MHz V^{-1}. Using this scaling factor k, the frequency detuning $\Delta\nu_{\mathrm{cg}} = k \times \Delta U_{\mathrm{cg}}$ can be calculated[11]. It is required to artificially shift one of the laser frequencies to observe both centers of gravity at the same acceleration voltage. With the shift applied to the anti-collinear laser frequency, the rest-frame transition frequency can be calculated by

$$\nu_0^2 = \nu_c \times (\nu_a + \Delta\nu_{\mathrm{cg}}), \tag{4}$$

where ν_a and ν_c are the doubled frequencies of the two locked dye lasers.

[11] The small error introduced by this linearization is insubstantial compared to the statistical and other sources of uncertainty and can be neglected.

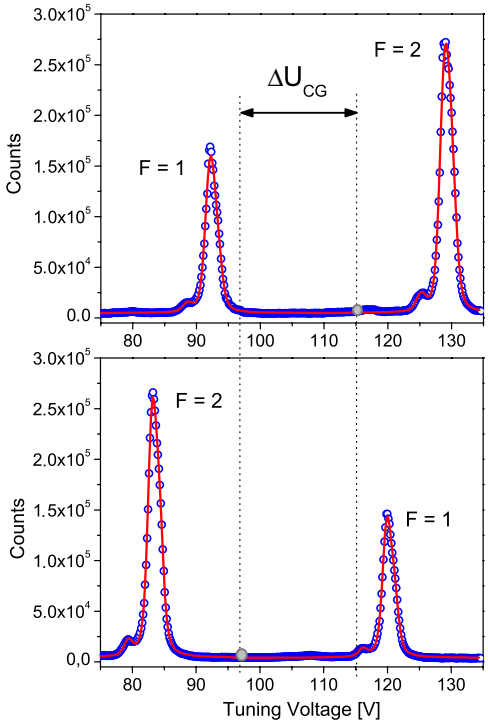

Figure 2. Collinear (top) and anti-collinear (bottom) spectrum recorded for the stable isotope ^{9}Be in the $2s_{1/2} \rightarrow 2s_{3/2}$ transition as a function of the Doppler tuning voltage applied to the detection region. The solid line is the overall fitting function with a Voigt profile for each peak.

The spectra of $^9Be^+$ were fitted with a multiple peak function containing all hyperfine transitions calculated from the nuclear spin and the atomic angular momentum. Each transition was fitted with a Voigt profile and common linewidth for all transitions. The small magnetic dipole and electric quadrupole interval factors $A_{2p_{3/2}}$ and $B_{2p_{3/2}}$ were taken from theoretical calculations [29]. They were introduced in the fitting routine as fixed parameters. The transition amplitudes were calculated relative to the strongest line according to the corresponding Racah intensity distributions. This procedure was necessary to ensure fitting results within physically meaningful constraints. In figure 2, a small peak on the left side of each hyperfine transition is visible. This peak arises from inelastic collisions of ions in the beam with residual gas atoms along the beamline. In such collisions Be^+ ions can be excited into the $2p$ states. The energy for this process is taken from the ions kinetic energy and is emitted in the form of a photon. Hence, those ions have resonance positions 3.97 eV below the main peak. This effect was included in the fitting function and was treated as an additional Voigt peak at a fixed distance from the main peak with identical relative intensities compared to the main peak of the respective hyperfine component.

In order to test the sensitivity of the resulting transition frequency to the unresolved hyperfine splitting and the particular lineshape model, ^{9}Be spectra obtained in collinear and anti-collinear excitation were also fitted independently with different lineshape functions. Besides the fit with fixed $2p_{3/2}$ hyperfine parameters described above, fits with single Voigt, Gaussian and Lorentzian profiles for each of the two hyperfine peaks, constrained to have

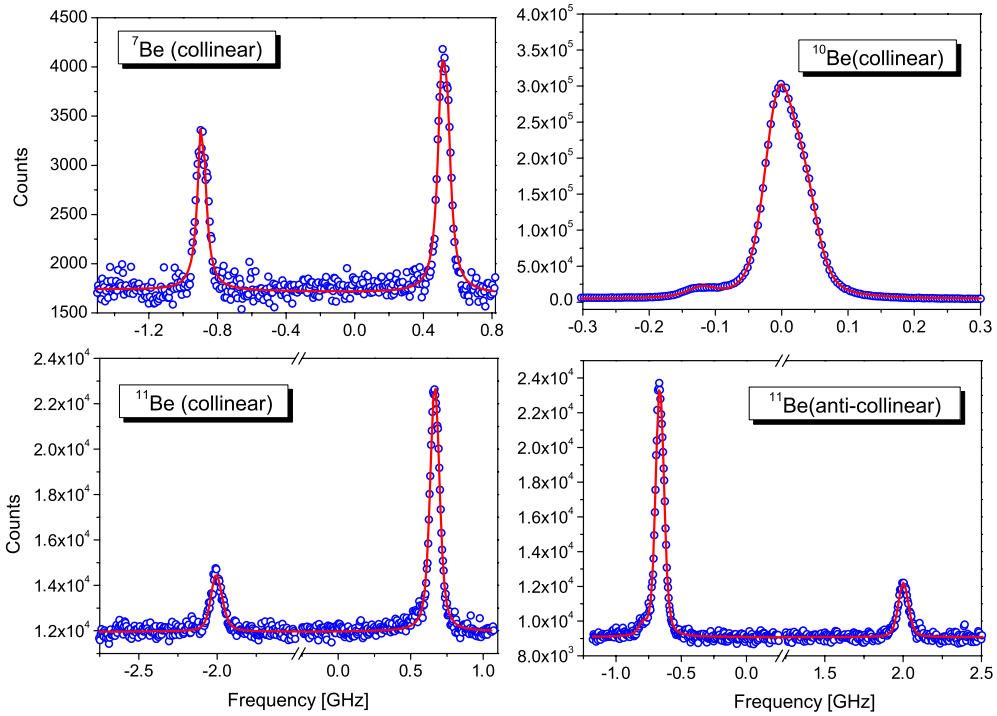

Figure 3. Spectra recorded for radioactive ^{7,10,11}Be isotopes in $2s_{1/2} \rightarrow 2p_{3/2}$ transition. Solid lines are Voigt fit functions. Frequencies are relative to the center of gravity of the respective isotope.

common line widths parameters, were performed. For each lineshape function, the cg frequencies were then combined to calculate the rest-frame frequency. The standard deviation of all measurements for one isotope was used as the statistical uncertainty of this value. The results for ν_0 obtained for the different lineshapes, scattered only by a fraction of this statistical uncertainty, indicating a negligible dependence on the chosen lineshape. Hence, the mean value of ν_0 obtained for the different lineshape functions was taken as the experimental transition frequency whereas the largest statistical uncertainty observed in the different fittings was kept as the final uncertainty.

For the radioactive isotopes a similar procedure was used. The spectra for ^{7,10,11}Be are shown in figure 3. Here the voltage axis is converted to a frequency scale. Solid lines show the fitting results with a Voigt line profile where the hyperfine splitting in the upper state was disregarded. A multi-line fit with individual hyperfine transitions as it was performed for ^{9}Be was only possible for ^{11}Be, since there is no information on the spectroscopic quadrupole moment of ^{7}Be and ^{10}Be does not exhibit any hyperfine structure ($I = 0$).

A special case is ^{10}Be, where the best counting statistics was obtained. For this isotope an additional asymmetry was observed in the line shapes. Such asymmetries shift the cg frequency in collinear and anti-collinear directions by approximately the same amount but with opposite sign in the frequency domain. Consequently, this contribution largely cancels when the rest-frame frequency ν_0 is calculated. Nevertheless, for comparison a third peak component beside the small inelastic collision contribution, residing on the higher frequency side of the resonance, was added to the fitting function, which resulted in a much better

Table 1. Extracted rms nuclear charge radii R_c from the $2s_{1/2} \rightarrow 2p_{3/2}$ (D_2) line compared to those obtained from the $2s_{1/2} \rightarrow 2p_{1/2}$ (D_1) transition [23]. Differences in the mean-square nuclear charge radii $\delta\langle r_c^2\rangle$ are calculated from isotope shifts $\delta\nu_{IS}^{9,A}$. The field shifts $\delta\nu_{FS}^{9,A}$ (reference isotope is ^{9}Be) are calculated using the theoretical mass shifts $\delta\nu_{MS}^{9,A}$ taken from the literature. Uncertainties of the absolute charge radii R_c from the D_2 and D_1 lines include the uncertainty of the reference radius $R_c(^9\text{Be}) = 2.519(12)$ fm [31].

Isotope	$\delta\nu_{IS}^{9,A}$ (MHz)	$\delta\nu_{MS}^{9,A}$ (MHz)	$\delta\nu_{FS}^{9,A}$ (MHz)	$\delta\langle r_c^2\rangle$ (fm^2)	$R_c(D_2)$ (fm)	$R_c(D_1)$ (fm)
^{7}Be	−49 242.1(2.0)	−49 231.827(39)[a]	−10.3(2.0)	0.61(12)	2.637(55)	2.647(17)
		−49 231.779(35)[b]				
^{10}Be	17 326.8(2.0)	17 312.569(13)[a]	14.2(2.0)	−0.87(12)	2.339(53)	2.357(18)
		17 312.553(13)[b]				
^{11}Be	31 568.8(2.3)	31 564.168(24)[a]	4.9(2.3)	−0.28(14)	2.463(62)	2.463(16)
		31 564.207(31)[b]				

[a] Reference [20].
[b] Reference [30].

description of the profile as it is shown in the spectrum of ^{10}Be in figure 3. The possible origin of this structure is not fully understood yet. While the individual peak position in collinear and anti-collinear spectra obtained from the fits of ^{10}Be$^+$ with one, two and three Voigt peaks differ by as much as 15 MHz, the rest-frame frequencies calculated by combining the collinear and anti-collinear results agree within 500 kHz. This clearly demonstrates the robustness of the collinear–anti-collinear approach with respect to the details of the lineshape function.

The isotope shifts relative to ^{9}Be were calculated from the fitting results and are listed in table 1. Using the precise mass-shift calculations from [20, 30] the field shift, which is proportional to the change in the mean-square nuclear charge radius, can be calculated by

$$\delta\langle r_c^2\rangle^{9,A'} = \frac{\delta\nu_{IS}^{9,A'} - \delta\nu_{MS}^{9,A'}}{C} \tag{5}$$

with the field shift constant $C \approx 17$ MHz fm^{-2}. For the data analysis more precise values for C taken from [21] were used, which show small isotopic variations. The rms nuclear charge radii were calculated based on the charge radius $R_c(^9\text{Be}) = 2.519(12)$ fm that was determined by elastic electron scattering [31]. A change of this reference charge radius would lead to a constant shift for all isotopes, not influencing the variations along the isotopic chain. The obtained rms charge radii as listed in table 1 are plotted in figure 4 and compared to the results from the $2s_{1/2} \rightarrow 2p_{1/2}$ transition. Both datasets agree very well within their uncertainties, but due to the resolved hyperfine structure in the D_1 line these previous values are slightly more precise.

Before we discuss the evaluated charge radii, a comparison between the isotope shifts in the D_1 and the D_2 transition should be made. These values are listed in table 2 and the difference between them is the so-called splitting isotope shift (SIS). The measured SIS are in a good agreement with the theoretical predictions but the uncertainties are still relatively large. An improved measurement of the isotope shift in the $2s_{1/2} \rightarrow 2p_{3/2}$ line, as it is planned at RIKEN [25, 32] with stored and laser-cooled ions in an RF ion trap, could clearly improve this comparison.

The best studied example for the SIS in a three-electron system is the lithium atom. Here, the value predicted from theory for the SIS between ^{6}Li and ^{7}Li is 0.396 MHz [20]. The most recent experimental values of −0.863(70) MHz [33] and 0.155(77) MHz [34] neither agree

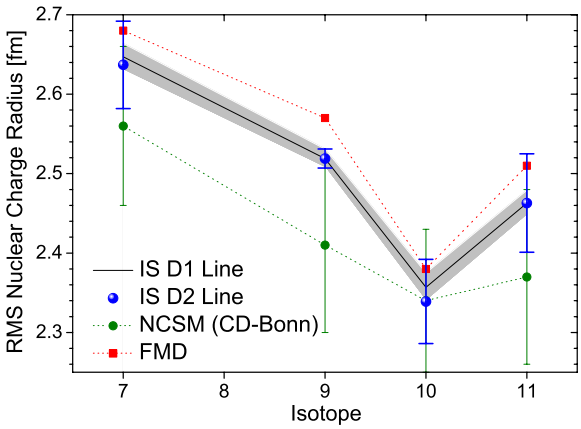

Figure 4. Nuclear charge radii of ^{7,9,10,11}Be obtained from isotope shift measurements, FMD multiconfiguration mixing calculations (FMD) and calculations in the no-core shell model (NCSM) with the CD-Bonn potential [26]. Radii extracted from the isotope shift in the D_1 line are represented by the black solid line and the gray area indicates the corresponding uncertainty. Radii extracted from the D_2 transition are shown as individual symbols with error bars.

Table 2. Experimental isotope shifts $\delta\nu_{\mathrm{IS}}^{9,A}$ (exp) in the $2s_{1/2} \rightarrow 2p_{1/2}$ (D_1) and $2s_{1/2} \rightarrow 2p_{3/2}$ (D_2) transitions and extracted splitting isotope shifts $\delta\nu_{\mathrm{SIS}}$ (exp). In the last two columns the values for $\delta\nu_{\mathrm{SIS}}$ from two independent theoretical calculations are listed. All values are given in MHz.

Isotope	$\delta\nu_{\mathrm{IS}}$ D_1 (exp)	$\delta\nu_{\mathrm{IS}}$ D_2 (exp)	$\delta\nu_{\mathrm{SIS}}$ (exp)	$\delta\nu_{\mathrm{SIS}}$ [29]	$\delta\nu_{\mathrm{SIS}}$ [20]
^{7}Be	−49 236.94(80)	−49 242.1(2.0)	−5.1(2.2)	−6.037(1)	−6.049
^{10}Be	17 323.82(82)	17 327.3(2.0)	3.5(2.4)	2.097(1)	2.13
^{11}Be	31 565.04(86)	31 569.6(2.3)	3.6(2.5)	3.965(1)	3.878

with each other nor with the predicted theoretical value. Therefore, the measured SIS for the $2p$ states in Be^+ is an important consistency check for theory and experiment.

4. Discussion

The charge radii presented here agree well with those reported earlier from our measurements in the D_1 transition [23]. There, we explained the general trend of the charge radii from ^{7}Be to ^{10}Be by the underlying cluster nature of these nuclei: the large nuclear charge radius of ^{7}Be ($= \alpha + {}^{3}$He) arises from the low cluster threshold of only 1.586 MeV, which implies an extended wavefunction for the relative motion of the clusters. While ^{8}Be ($= \alpha + \alpha$) is unbound, the additional neutron in ^{9}Be glues together the two α particles with a relatively small binding energy of only 1.573 MeV, which is reflected again in a correspondingly large charge radius. ^{10}Be, on the other hand, is well bound and the nucleus is stiff against a variation in the distance of the α clusters. The additional neutron in ^{11}Be can either occupy a $1p_{1/2}$ orbit (in the excited $1/2^-$ state at 320 keV) or an orbit in the $2s_{1/2}$ shell for the $1/2^+$ ground state. The experimental binding energy is only 504 keV and an extended halo is expected. Even if the core is not polarized the charge radius will change, as the ^{10}Be core will move with respect to the center of mass of the nucleus, according to

$$R_c^2(^{11}\mathrm{Be}) = R_c^2(\mathrm{core}) + \tfrac{1}{11^2} R_{\mathrm{core}-n}^2 + \tfrac{1}{4} R_n^2, \tag{6}$$

Table 3. Root-mean-square nuclear charge radii R_c for beryllium isotopes obtained from different theoretical calculations (th) and isotope shift measurements IS (exp). Experimental charge radii are the weighted averages of the values attained from the D_1 [23] and D_2 transitions (this work). All values are given in fm.

Isotope	FMD (th)	NCSM (th)	GFMC (th)	IS (exp)
^{7}Be	2.68	2.56(10)	2.588	2.646(16)
^{9}Be	2.57	2.41(11)	2.520	2.519(12)
^{10}Be	2.38	2.34(9)	2.354	2.355(17)
^{11}Be	2.51	2.37(11)	–	2.463(15)

FMD—fermionic molecular dynamics (this work).
NCSM—no core shell model with the CD-Bonn potential [26].
GFMC—Green's function Monte Carlo calculations [37, 38].

with the core–neutron distance being $R_{\mathrm{core}-n}$ and the mean-square charge radius of the neutron $R_n^2 = -0.117(4)$ fm^2 [35]. In the following, we will discuss conclusions to be drawn from the combination of our results with other experiments and present details of fermionic molecular dynamics calculations on the beryllium isotopes.

Using the charge radii extracted from the D_1 transition, listed in table 1, and assuming that there is no polarization of the ^{10}Be core we obtain $R_{\mathrm{core}-n} = 8.09(1.22)$ fm. To get an idea how far the assumption of the absence of core polarization is valid, this number can be compared with data from electromagnetic and nuclear inelastic scattering on ^{11}Be: by measuring the one-neutron removal channel, a radius for the valence neutron of 5.7(4) fm was deduced [36]. With this value, the center-of-mass motion of ^{10}Be would result in a ^{11}Be charge radius slightly smaller than observed in our measurements and an additional increase of the core charge radius to 2.41(2) fm is required to explain the experimental ^{11}Be charge radius. Hence, the charge radius of the core is expected to be about 2.2(1.8)% larger than that of the free ^{10}Be nucleus.

In our previous publication [23], we compared the experimental data to theoretical predictions from *ab initio* calculations in the Green's Function Monte Carlo (GFMC) approach [37, 38] (no result for ^{11}Be is so far available), no-core shell model (NCSM) calculations and the fermionic molecular dynamics (FMD) approach. Here, we compare them with updated NCSM results [26] using the CD-Bonn interaction and present new FMD calculations. Nuclear charge radii obtained from these theoretical models are shown in figure 4. Error bars for the NCSM radii were estimated based on the model space size and the oscillator frequency dependence [26]. Charge radii obtained with the INOY interaction, which provides binding energies closer to experiment than the CD-Bonn interaction, are significantly smaller and outside the CD-Bonn error bars. Although the charge radii are in general too small, the NCSM calculations are able to describe the decrease from ^{7}Be to ^{10}Be but they show only a small increase for the ^{11}Be charge radius. This is a deficiency of the NCSM model space which has difficulties to properly describe the neutron halo in ^{11}Be. This problem is now being attacked by coupling the NCSM with the cluster model [39]. Root-mean-square nuclear charge radii obtained from theoretical calculations and isotope shift measurements are listed in table 3.

5. Fermionic molecular dynamics

Fermionic molecular dynamics (FMD) [40] is a many-body approach especially suited for the description of nuclei with cluster or halo structure. It has been used successfully to describe form factors and charge radii of light nuclei in the *p* shell and *sd* shell [22, 41]. In

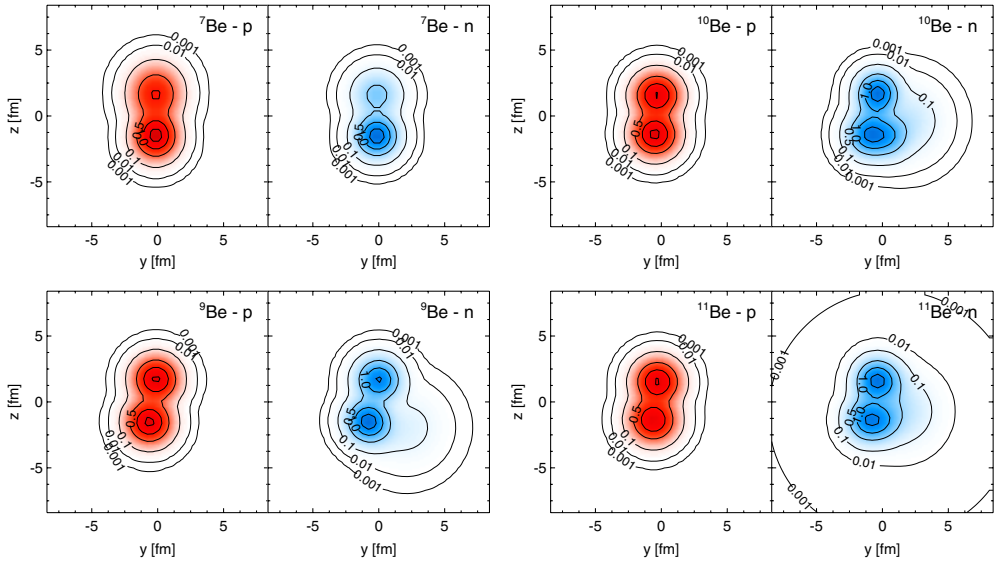

Figure 5. Cuts through the proton and neutron densities of the intrinsic states obtained in FMD VAP calculations. Contour lines are in units of half nuclear matter density.

the present calculation the intrinsic many-body basis states are given by Slater determinants $\left|Q\right\rangle$ using a superposition of two Gaussian wave packets for each single-particle state. The parameters of the wave packets are mean position, mean momentum, width and orientation of the spin. The basis is very flexible; it contains the harmonic oscillator shell model states as well as Brink-type cluster model states as limiting cases. The variable width parameter allows an efficient description of spatially extended nucleon wavefunctions as appearing in halo nuclei. To restore the symmetries of the Hamiltonian, the Slater determinant is projected on parity, angular momentum and total linear momentum $|Q;\, J^{\pi} MK,\, \vec{P} = 0\rangle$. Diagonalizing the Hamiltonian in the basis spanned by different K quantum numbers provides the states $|Q;\, J^{\pi} M\kappa,\, \vec{P} = 0\rangle$ which are used as many-body basis states.

The effective interaction is based on V_{UCOM} derived from the realistic Argonne V18 interaction by the explicit treatment of short-range central and tensor correlations in the unitary correlation operator method [42]. It also includes a phenomenological two-body correction term that has been fitted to the binding energies and radii of doubly-magic nuclei up to ^{48}Ca. No parameters have been adjusted for the beryllium isotopes.

The parameters of the wavefunction were obtained by the variation of the energy after projection (VAP) on parity and angular momentum. In figure 5 cuts through the proton and neutron densities of the intrinsic states are shown. In contrast to mean field calculations the intrinsic states obtained in VAP calculations show a pronounced α-clustering (α particle—^{3}He in the case of ^{7}Be). As the cluster thresholds, especially in ^{7}Be and ^{9}Be, are low, we expect an extended wavefunction for the relative motion of the clusters. Already in a single Slater determinant the relative distance of the clusters has a Gaussian distribution, but for a realistic description a superposition of several many-body states is needed. We generated such many-body states by imposing constraints on the distance between the clusters. A good measure for the distance of the clusters (assuming no significant polarization of the clusters) is the rms radius of the proton distribution with respect to the center of charge (R_{pp}). This is different from the charge radius which measures the proton radius with respect to the center of mass

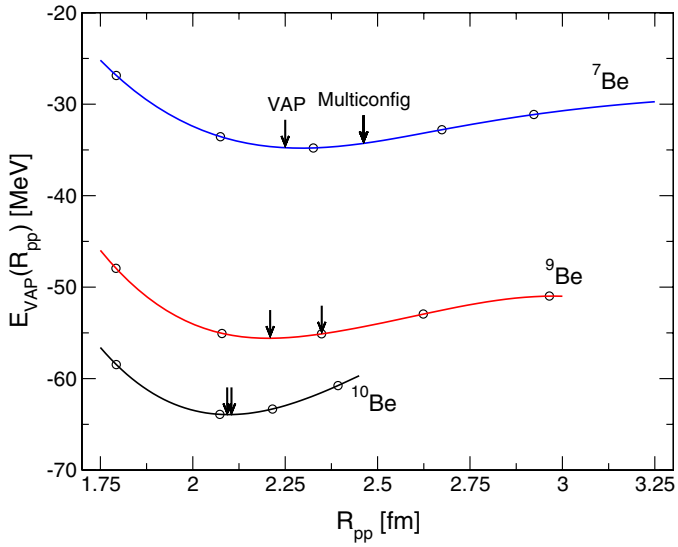

Figure 6. Energies of FMD configurations for ^{7,9,10}Be obtained in variation after projection (VAP) calculations. The proton radius with respect to the center of charge R_{pp} is used as a constraint for the intrinsic state. Arrows indicate the R_{pp} expectation values obtained in the VAP minimum and from multiconfiguration mixing calculations.

and which is therefore sensitive not only to the distance of the clusters but also to the motion of the clusters relative to the center of mass.

For each nucleus we performed VAP calculations with a constraint on the radius R_{pp} of the intrinsic states. In figure 6 the energies are shown as a function of R_{pp}. The energy surfaces are very flat for ^{7}Be and ^{9}Be. Therefore, configurations with large R_{pp} will contribute to the ground state and will also increase the charge radius significantly compared to the VAP calculation using a single configuration. In ^{10}Be, on the other hand, the energy surface is rather steep and extended configurations will not significantly contribute to the ground state. Assuming no polarization of the clusters the R_{pp} values can be translated into the rms cluster distances of 4.23 fm (^{7}Be), 4.08 fm (^{9}Be) and 3.51 fm (^{10}Be).

For ^{11}Be the situation is different. The neutron separation energy is very small and as might be expected the FMD configuration obtained in the unconstrained VAP calculation essentially corresponds to the ^{10}Be VAP state plus an additional neutron in an extended *s*-orbit. Whereas R_{pp} is almost identical in the ^{10}Be and ^{11}Be VAP states, the charge radius increases significantly. This is due to the motion of the ^{10}Be core with respect to the total center of mass. For an improved description of ^{11}Be we did not only use the R_{pp} constraint which affects mainly the ^{10}Be core but also varied a second many-body state in a multiconfiguration calculation for each R_{pp}. By this procedure configurations with a ^{10}Be core in the 2^{+} state and the valence neutron occupying a *d*-orbit are included. This admixture of core polarized configurations improves the ^{11}Be binding energy by about 1 MeV and is necessary to get ^{11}Be bound with respect to ^{10}Be. It leads to a slight increase of R_{pp} from 2.10 fm in ^{10}Be to 2.19 fm in ^{11}Be. However, the effect on the charge radius of the ^{10}Be core is very small, it changes from 2.52 fm to 2.51 fm.

In summary, all FMD charge radii are slightly too large compared to the experimental results (see figure 4) but capably reproduce the systematic trend. The FMD calculations

presented in [23] did not include configurations with large cluster distances and therefore smaller radii, especially for ^{7}Be and ^{9}Be, were obtained. Absolute charge radii values deduced from $\delta\langle r_c^2\rangle$ furthermore depend on the reliability of $R_c(^{9}\mathrm{Be})$ from electron scattering data, which should be kept in mind in comparison with theory.

To conclude, we have measured the isotope shifts in the $2s_{1/2} \rightarrow 2p_{3/2}$ transition of Be^{+} and extracted the nuclear charge radii for ^{7,10,11}Be. The radii were compared to results of our previous measurement in the $2s_{1/2} \rightarrow 2p_{1/2}$ transition and good agreement was found. When combined with results from the electromagnetic and nuclear inelastic scattering of ^{11}Be, a small 2.2(1.8)% charge-radius increase of the core in ^{11}Be compared to the free ^{10}Be nucleus can be deduced. Results are also compared to calculations in the fermionic molecular dynamics approach which were able to explain their systematic behavior. Thus, it can be concluded from theory and experiment that the dominant contribution to the change in the charge radius between ^{10}Be and ^{11}Be is the center-of-mass motion of the ^{10}Be core caused by the halo neutron, whereas the contribution of core polarization is rather small. Additionally, the splitting isotope shift in the $2p$ states was evaluated, showing good consistency with theoretical predictions.

Acknowledgments

This work was supported by the Helmholtz Association (VH-NG-148), BMBF (06TU263I, 06MZ215, 06UL264I), and the EU (FP-6 EU RII3-CT-2004-506065), MK was supported by the EU (MEIF-CT-2006-042114). We gratefully acknowledge support by M Fischer and R Holzwarth from Menlo Systems and the ISOLDE technical group. We thank K Pachucki and M Puchalski for stimulating discussions and for providing their calculated D_2 mass shifts prior to publication.

References

[1] Tanihata I *et al* 1985 *Phys. Lett.* B **160** 380
[2] Brohm T *et al* 1991 *GSI Sci. Rep. 1990* **91–1** 12
[3] Webber W R *et al* 1990 *Phys. Rev.* C **41** 520
[4] Blank B *et al* 1992 *Z. Phys.* A **343** 375–9
[5] Chulkov L *et al* 1996 *Nucl. Phys.* A **603** 219–37
[6] Chulkov L *et al* 2000 *Nucl. Phys.* A **674** 330–42
[7] Hansen P G and Jonson B 1987 *Europhys. Lett.* **4** 409
[8] Jonson B 2003 *Phys. Rep.* **389** 1–59
[9] Otten E W 1989 *Treatise Heavy Ion Sci.* **8** 515
[10] Arnold E *et al* 1987 *Phys. Lett.* B **197** 311
[11] Geithner W *et al* 1999 *Phys. Rev. Lett.* **83** 3792
[12] Arnold E *et al* 1992 *Phys. Lett.* B **281** 16
[13] Borremans D *et al* 2005 *Phys. Rev.* C **72** 044309
[14] Neugart R *et al* 2008 *Phys. Rev. Lett.* **101** 132502
[15] Mueller P *et al* 2007 *Phys. Rev. Lett.* **99** 252501
[16] Sánchez R *et al* 2006 *Phys. Rev. Lett.* **96** 033002
[17] Yan Z-C and Drake G W F 2000 *Phys. Rev.* A **61** 022504
[18] Yan Z-C and Drake G W F 2003 *Phys. Rev. Lett.* **91** 113004
[19] Puchalski M, Moro A M and Pachucki K 2006 *Phys. Rev. Lett.* **97** 133001
[20] Yan Z C, Noertershaeuser W and Drake G W F 2008 *Phys. Rev. Lett.* **100** 243002
[21] Puchalski M and Pachucki K 2008 *Phys. Rev.* A **78** 052511
[22] Geithner W *et al* 2008 *Phys. Rev. Lett.* **101** 252502
[23] Noertershaeuser W *et al* 2009 *Phys. Rev. Lett.* **102** 062503
[24] Geppert C *et al* 2010 to be published
[25] Nakamura T *et al* 2006 *Phys. Rev. Lett.* **96** 252502

[26] Forssén C, Caurier E and Navrátil P 2009 *Phys. Rev.* C **79** 021303
[27] Sánchez R *et al* 2009 *Can. J. Phys.* **87** 825
[28] Thuemmler T, Marx R and Weinheimer Ch 2009 *New J. Phys.* **11** 103007
[29] Puchalski M and Pachucki K 2009 *Phys. Rev.* A **79** 032510
[30] Puchalski M 2009 private communication
[31] Jansen J A, Peerdeman R T and De Vries C 1972 *Nucl. Phys.* A **188** 337
[32] Takamine A *et al* 2009 *Eur. Phys. J.* A **42** 369
[33] Das D and Natarajan V 2007 *Phys. Rev.* A **75** 052508
[34] Noble G A, Schultz B E, Ming H and van Wijngaarden W A 2006 *Phys. Rev.* A **74** 012502
[35] Kopecky S *et al* 1997 *Phys. Rev.* C **56** 2229
[36] Palit R *et al* 2003 *Phys. Rev.* C **68** 034318
[37] Pieper S C and Wiringa R B 2001 *Ann. Rev. Nucl. Part. Sci.* **51** 53–90
[38] Pieper S C, Varga K and Wiringa R B 2002 *Phys. Rev.* C **66** 044310
[39] Quaglioni S and Navrátil P 2009 *Phys. Rev.* C **79** 044606
[40] Neff T and Feldmeier H 2008 *Eur. Phys. J. Spec. Top.* **156** 69
[41] Chernykh M *et al* 2007 *Phys. Rev. Lett.* **98** 032501
[42] Neff T and Feldmeier H 2003 *Nucl. Phys.* A **713** 311